











Cite this: *RSC Adv.*, 2024, 14, 34457

# Facile synthesis of a 3D magnetic graphene oxide/ $\text{Fe}_3\text{O}_4$ /banana peel-derived cellulose composite aerogel for the efficient removal of tetracycline

Lam-Tuan-Cuong Dang, <sup>ab</sup> Hoang-Vinh-Truong Phan, <sup>cd</sup> Minh-Trung Dao, <sup>e</sup> Thanh-Truc Dang, <sup>f</sup> Soontorn Suvokhiaw, <sup>g</sup> Nhan-Tam Do, <sup>h</sup> Thi-Anh-Minh Nguyen, <sup>ij</sup> Van-Kieu Nguyen <sup>\*cd</sup> and Le-Thuy-Thuy-Trang Hoang <sup>\*ab</sup>

Many initiatives have incorporated graphene oxide (GO) and biomass into aerogels for wastewater treatment. We report on the facile fabrication of a magnetic  $\text{GO}/\text{Fe}_3\text{O}_4$ /banana peel-derived cellulose (bio-cellulose) aerogel using an ultrasound-assisted mechanical mixing method and freeze-drying technique for the removal of tetracycline (TC). The component materials and composite aerogel were characterized using Fourier-transform infrared spectroscopy (FTIR), X-ray powder diffraction (XRD), Raman spectroscopy, field-emission scanning electron microscopy (FE-SEM), energy-dispersive X-ray spectroscopy (EDX), nitrogen adsorption-desorption analysis, and vibrating sample magnetometry (VSM). The effects of solution pH and adsorbent dose on the adsorption performance of the synthesized adsorbents were investigated. The adsorption behavior at the equilibrium of the  $\text{GO}/\text{Fe}_3\text{O}_4$ /bio-cellulose aerogel was studied and analyzed using four well-known non-linear models: Langmuir, Freundlich, Sips, and Temkin. The results showed that the experimental data fitted well with the Freundlich and Sips isotherm models. The maximum adsorption capacity achieved from the Sips model was  $238.7 \text{ mg g}^{-1}$ . The adsorption kinetics were studied and proved to follow the Elovich kinetic model with an initial rate of  $0.89 \text{ g g}^{-1} \text{ min}^{-1}$ . These results confirm the favorable adsorption of TC on the heterogeneous surface that exhibits a wide range distribution of adsorption energies of the desired  $\text{GO}/\text{Fe}_3\text{O}_4$ /bio-cellulose aerogel. The experimental findings demonstrate that the aerogel possesses the notable features of environmental friendliness, cost-effectiveness, and comparatively high TC adsorption capacity. Therefore, utilizing biomass to develop the structure of the magnetic GO-based composite aerogel is significantly promising for antibiotic-containing wastewater treatments.

Received 8th July 2024  
Accepted 21st October 2024

DOI: 10.1039/d4ra04942j

rsc.li/rsc-advances

## 1 Introduction

In recent years, water contamination with inorganic and organic pollutants derived from diverse industrial activities,

agricultural practices, and domestic waste has become a severe global concern, jeopardizing aquatic biota and posing a direct threat to human health, such as through waterborne diseases.<sup>1–5</sup> Noticeably, antibiotics have been overused in human medicine, animal husbandry, and aquaculture since the introduction of penicillin in 1928.<sup>6–8</sup> The massive annual consumption of antibiotics worldwide results in the constant release into aquatic media, escalating water contamination.<sup>7,9</sup> Tetracycline (TC) is one of the most commonly prescribed antibiotics owing to its potent antimicrobial properties.<sup>10–12</sup> However, TC is only partially metabolized in the bodies of humans and animals, and its residue is mainly excreted into the environment through urine and feces.<sup>12–15</sup> The tough degradation and eco-toxicity of this residue remaining in agricultural runoff and municipal sewage can cause accumulation and pollution in soil and water.<sup>11,16</sup> Hence, removing TC from aqueous media is an imperative task for protecting and enhancing ecosystem and public health.<sup>9</sup> There are numerous approaches to eliminate TC, such as membrane filtration, sludge treatment, adsorption, electrochemical routes, and advanced oxidation methods.<sup>7,9,10,17</sup>

<sup>a</sup>Laboratory of Advanced Materials Chemistry, Institute for Advanced Study in Technology, Ton Duc Thang University, Ho Chi Minh City, Vietnam. E-mail: hoanglethuythuytrang@tdtu.edu.vn

<sup>b</sup>Faculty of Applied Sciences, Ton Duc Thang University, Ho Chi Minh City, Vietnam

<sup>c</sup>Institute of Fundamental and Applied Sciences, Duy Tan University, Ho Chi Minh 700000, Vietnam. E-mail: nguyenvankieu2@duytan.edu.vn

<sup>d</sup>Faculty of Natural Sciences, Duy Tan University, Da Nang 550000, Vietnam

<sup>e</sup>Department of Environmental Engineering, Thu Dau Mot University, Thu Dau Mot City, Binh Duong, 820000, Vietnam

<sup>f</sup>Graduate University of Science and Technology, Vietnam Academy of Science and Technology, Ha Noi, Vietnam

<sup>g</sup>Department of Chemistry, Faculty of Science, Silpakorn University, Nakhon Pathom 73000, Thailand

<sup>h</sup>Faculty of Natural Science Education, Dong Nai University, Dong Nai, Vietnam

<sup>i</sup>Institute of Research and Development, Duy Tan University, Da Nang, Vietnam

<sup>j</sup>School of Engineering & Technology, Duy Tan University, Da Nang, Vietnam



In particular, adsorption is considered one of the simple, affordable, and manageable measures to separate contaminants from wastewater.<sup>9,18</sup> Accordingly, a wide range of adsorbents, including carbonaceous materials,<sup>19–24</sup> zeolites,<sup>25–27</sup> magnetite nanoparticles,<sup>28–30</sup> clay minerals,<sup>31–33</sup> and polymeric resins<sup>34,35</sup> have been investigated for the removal of TC. Among these materials, GO-based composite aerogel has been emerging as a promising adsorbent for the removal of various pollutants.<sup>36–38</sup>

The use of GO-based composites can do wonders for a wide range of benefits in wastewater treatments. GO is a commonly used derivative of graphene with the advantage of low-cost production compared to pristine graphene.<sup>5</sup> Graphene is a single layer of carbon atoms bonded in a two-dimensional (2D) honeycomb lattice structure.<sup>39</sup> GO has a similar structure to graphene with the presence of oxygen-containing functional groups, such as epoxy, hydroxyl, carbonyl, and carboxyl groups.<sup>40</sup> GO has aroused widespread attention in pollution mitigation and environmental remediation due to its unique physicochemical properties, such as high mechanical and chemical stabilities, excellent electrical and thermal conductivity, large specific surface area, high optical transparency, low density, and flexibility to incorporate various materials.<sup>41</sup> The presence of ample oxygen-containing functional groups in GO and its hydrophilic property allows an easy dispersion of this material in aqueous solutions and effective interactions with various water-soluble compounds, enabling GO to become a valuable material for adsorption applications.<sup>4,5,16,41</sup> This characteristic, however, complicates the complete recovery of the material from aqueous media due to the formation of colloidal suspension.<sup>38,42</sup> Moreover, using GO in various applications has faced difficulties arising from the phenomena of restacking and aggregation of 2D sheets, thereby reducing their activity and reusability.<sup>7,43,44</sup> Thus, the development of three-dimensional (3D) materials such as foams or aerogels based on the 2D structure of GO has been designed to address these issues.<sup>7,45,46</sup> The 2D sheets of GO are immobilized into 3D structures by forming interconnected networks, resulting in more stable, bulky, and porous materials.<sup>47,48</sup> Therefore, this eases the handling and the regeneration of the materials while the hydrophilic feature is still retained for functionalities or other chemical interactions.<sup>49</sup> Furthermore, the combination of magnetite and GO to produce magnetic GO-based composites is beneficial for a rapid separation from the matrix using an external magnetic field.<sup>50,51</sup>

To date, the aerogel forms of magnetic GO-based composites have been universally prioritized for the elimination of contaminants among 3D GO-based composite existences for a variety of reasons.<sup>42,43,52</sup> Specifically, aerogel is an ultra-light 3D porous material with exceptional properties, such as an extremely low density, a huge porosity, and a vast specific surface area.<sup>53,54</sup> These features facilitate the adsorption of diverse pollutants while flexibly incorporating various components to create purpose-driven multifunctional materials.<sup>2,55</sup> GO is one of the most appropriate precursor materials to satisfy such features, based on its possession of rich hydrophilic functionalities.<sup>4</sup> These functional groups can interact with

various other hydrophilic agents through hydrogen bonding,  $\pi$ - $\pi$  bonding, or electrostatic interactions to immobilize 2D sheets of GO and create 3D structured aerogel.<sup>5,41,55</sup> The skeletons for building 3D aerogel can be sodium alginate,<sup>56</sup> cellulose,<sup>2</sup> and ethylene diamine.<sup>57</sup> Among them, cellulose is usually employed by virtue of its abundance and rich functionalities.<sup>58</sup>

Cellulose can be harnessed from various natural resources, such as plants, bacteria, algae, and tunicates.<sup>59</sup> Recently, biomass waste-derived cellulose has garnered significant interest in the development of eco-friendly and biocompatible fibers supporting 3D aerogel.<sup>60,61</sup> This aligns with the principles of green chemistry and sustainable development in wastewater treatment practices.<sup>60</sup> Repurposing these materials for adsorbent production contributes to sustainability by utilizing abundant resources instead of throwing them away, alleviating the environmental impact associated with waste disposal.<sup>62,63</sup> Agro-waste materials such as banana peels are readily available in large quantities. Not only are banana peels one of the most abundant agro-waste worldwide, but they are also composed of hemicellulose, cellulose, and lignin, helping them become an ideal selection of inexpensive and bio-based adsorbents for wastewater treatment.<sup>61,64,65</sup> The plentiful oxygen-containing functional groups in bio-cellulose provide extraordinary structure for developing 3D aerogel while expectedly upgrading the adsorption capacity.<sup>66</sup>

This study aims to integrate GO, magnetic  $\text{Fe}_3\text{O}_4$ , and bio-cellulose into an ultralight 3D composite aerogel using an ultrasound-assisted mechanical mixing method and freeze-drying technique for the removal of TC. This approach was expected to fully utilize the strengths of each component in the composite aerogel, including the magnetic property of  $\text{Fe}_3\text{O}_4$  for easy separation of the aerogel after use, the skeletal property of bio-cellulose, and the potential adsorption sites of both GO and bio-cellulose.

## 2 Experimental

### 2.1 Chemicals and materials

Graphite powder (Gi, particle size < 20  $\mu\text{m}$ ) was procured from Sigma-Aldrich Co. Ltd in Germany. Potassium permanganate ( $\text{KMnO}_4$ , 99%), sulfuric acid ( $\text{H}_2\text{SO}_4$ , 98%), phosphoric acid ( $\text{H}_3\text{PO}_4$ , 85%), iron(II) sulfate heptahydrate ( $\text{FeSO}_4 \cdot 7\text{H}_2\text{O}$ , 99%), iron(III) chloride hexahydrate ( $\text{FeCl}_3 \cdot 6\text{H}_2\text{O}$ , 99%), ammonia solution ( $\text{NH}_4\text{OH}$ , 30%), hydrogen peroxide ( $\text{H}_2\text{O}_2$ , 30%), sodium hypochlorite ( $\text{NaOCl}$ , 30%), and ethanol ( $\text{C}_2\text{H}_5\text{OH}$ , 99%) were obtained from Xilong Scientific Co. Ltd in China and employed without additional purification. Cavendish banana peels were collected from the local markets in District 12, Ho Chi Minh City, Vietnam. Distilled water was used in the experiment.

### 2.2 Synthesis of GO suspension

GO was produced using the modified Hummers' method.<sup>67</sup> In brief, 3 g of Gi was incrementally added to an acid mixture comprising 360 mL of 98%  $\text{H}_2\text{SO}_4$  and 40 mL of 85%  $\text{H}_3\text{PO}_4$  while being continuously stirred at a temperature below 20  $^\circ\text{C}$ .



Next, 18.0 g of  $\text{KMnO}_4$  was slowly supplemented to the mixture, heated to 50 °C, and stirred continuously for 12 h. Subsequently, 500 mL distilled water and 15 mL  $\text{H}_2\text{O}_2$  were gently added to the solution to cease the oxidation reactions. Centrifugation and washing with distilled water were carried out alternately until the neutral pH of the decanted water was obtained. The centrifugation was carried out at 6000 rpm on the Hettich EBA 21 centrifuge with a 6-place angle rotor. The resulting residue was subjected to drying at 60 °C for 24 h, yielding solid graphite oxide. This solid was then dissolved in distilled water at a concentration of 2 mg  $\text{mL}^{-1}$ , followed by sonication at 360 W until obtaining the GO colloidal suspension.

### 2.3 Synthesis of magnetic $\text{Fe}_3\text{O}_4$

$\text{Fe}_3\text{O}_4$  particles were synthesized following the method detailed by Hoang *et al.*<sup>68</sup> Briefly, 25 mL of 1.38 M  $\text{Fe}^{2+}$  solution and 25 mL of 2.76 M  $\text{Fe}^{3+}$  solution were combined to achieve the  $\text{Fe}^{2+} : \text{Fe}^{3+}$  molar ratio of 1 : 2. Subsequently, ammonia solution 30% was added to the mixture until the pH reached 10.0. After stirring for 1 h, the resulting black precipitates were separated using an external magnet and rinsed thrice with distilled water. The synthesized  $\text{Fe}_3\text{O}_4$  particles were then dried at 60 °C for 12 hours.

### 2.4 Isolation of cellulose from banana peels

The bio-cellulose was isolated from banana peels *via* alkali treatment and then acid hydrolysis.<sup>2,69</sup> Banana peels were cut into small pieces and washed with distilled water. These small pieces were immersed into a 3 M NaOH solution and heated at 70 °C for 4 h to remove lignin and hemicellulose. Afterward, the pieces were filtered and washed with distilled water until they had a neutral pH. The remaining solid was bleached using 2% NaClO at 80 °C for 2 h. Subsequently, the bleached product was washed with distilled water and hydrolyzed with  $\text{H}_2\text{SO}_4$  40% at 80 °C for 2 h, then rinsed with distilled water until reaching the neutral pH of the decanted water. The bio-cellulose was separated by centrifugation at 6000 rpm on the Hettich EBA 21 centrifuge with the 6-place angle rotor and stored in a refrigerator for further use.

### 2.5 Preparation of magnetic $\text{GO}/\text{Fe}_3\text{O}_4/\text{bio-cellulose}$ aerogel

Magnetic  $\text{Fe}_3\text{O}_4$  particles were dispersed in the GO colloidal suspension (2 mg  $\text{mL}^{-1}$ ) in an ultrasound bath for 30 min, in which the mass ratio of  $\text{Fe}_3\text{O}_4$  to GO was 1 : 1.<sup>3</sup> Subsequently, the bio-cellulose was added to the mixture with a double amount of GO mass under the sonication at 360 W for 30 min.<sup>2</sup> The resulting mixture was then placed in a water bath at 90 °C for 6 h to yield  $\text{GO}/\text{Fe}_3\text{O}_4/\text{bio-cellulose}$  hydrogel and freeze-dried at −40 °C for 48 h to obtain the magnetic  $\text{GO}/\text{Fe}_3\text{O}_4/\text{bio-cellulose}$  aerogel.

### 2.6 Characterization

The functional groups of materials were identified through FTIR spectra analysis using Jasco FT/IR-6X spectrometer (Jasco,

Tokyo, Japan) with ATR-FTIR mode, within the wavenumber range of 500–4000  $\text{cm}^{-1}$ . Raman spectroscopy was recorded at an excitation wavelength of 532 nm by Labram, Horiba spectroscopy. The crystalline structure of materials was examined using X-ray powder diffraction (D8 Advance X-ray diffractometer) with  $\text{CuK}\alpha$  irradiation ( $\lambda_x = 0.154$  nm) in the  $2\theta$  range of 5–80° (0.02° per second). The surface morphology of the materials and elemental mapping were monitored by FE-SEM (TESCAN MIRA3, Czech Republic) equipped with EDX (EDAX, AMETEK) at an accelerating electron voltage of 15.0–20.0 kV, capturing both top view and cross-section view. The specific surface area of materials was measured using the Brunauer–Emmett–Teller method (BET) with Micromeritics MicroActive for TriStar II Plus 2.03 surface area analyzer through  $\text{N}_2$  adsorption at 77.3 K, pretreated at 120 °C before measurement. The magnetic hysteresis loops were plotted by an in-house developed VSM system under ambient conditions.

### 2.7 Point of zero charge ( $\text{pH}_{\text{pzc}}$ ) determination

To determine the  $\text{pH}_{\text{pzc}}$  of the magnetic  $\text{GO}/\text{Fe}_3\text{O}_4/\text{bio-cellulose}$  aerogel, the solid addition method was deployed based on the method of Hoang *et al.*<sup>70,71</sup> Initially, a set of flasks containing 30 mL of 0.1 M  $\text{KNO}_3$  solution was prepared, with the initial pH ( $\text{pH}_i$ ) ranging from 3.0 to 9.0. The pH was adjusted using 0.1 M HCl and 0.1 M NaOH. Subsequently, 50 mg of the as-prepared aerogels was added and shaken at 150 rpm for 24 h until reaching equilibrium. The equilibrium pH ( $\text{pH}_e$ ) was recorded to determine the deviation compared to  $\text{pH}_i$ , denoted as  $\Delta\text{pH} = \text{pH}_i - \text{pH}_e$ . Finally, a plot of  $\Delta\text{pH}$  as a function of  $\text{pH}_i$  was constructed, and the  $\text{pH}_{\text{pzc}}$  was measured at the intersection point between the axis (at  $\Delta\text{pH} = 0$ ) and the resulting curve.

### 2.8 Adsorption studies

Batch adsorption investigations were conducted to assess the efficiency of the magnetic  $\text{GO}/\text{Fe}_3\text{O}_4/\text{bio-cellulose}$  aerogel in removing TC from aqueous solutions. The experimental design involved a one-factor system in which the effect of one factor was investigated at different values while keeping constant for other factors. Specifically, 15 mg of each aerogel was prepared for immersing into Erlenmeyer flasks containing 30 mL TC solutions, meaning the solid-to-liquid ratio of 1 : 2. The solutions were then shaken at 160 rpm and at ambient temperature. After continuous shaking for a specific duration, the aerogels were collected by the external magnet, and the equilibrium TC concentration was determined *via* the analysis of UV-Vis spectra at 357 nm. The investigated factors and corresponding experimental conditions are outlined in Table 1. The adsorption capacity ( $q_e$ , mg  $\text{g}^{-1}$ ) of the aerogels was calculated using eqn (1):

$$q_e = \frac{(C_0 - C_e)V}{M} \quad (1)$$

where  $C_0$  and  $C_e$  are the initial and equilibrium concentrations of TC (mg  $\text{L}^{-1}$ ), respectively;  $M$  is the aerogel mass (g); and  $V$  is the volume of TC solution (L).



**Table 1** Experimental conditions in batch adsorption studies for TC removal

Factors	Studied values	Experimental conditions
pH	3.0, 4.0, 5.0, 6.0, 7.0, 8.0, 9.0, 10.0 <sup>a</sup>	Adsorbent dose: 0.5 g L <sup>-1</sup> Initial TC concentration: 70 mg L <sup>-1</sup> Adsorption time: 16 h
Adsorbent dose (g L <sup>-1</sup> )	0.50, 0.67, 0.83, 1.0, 1.17, 1.33	Solution pH: 5.0 Initial TC concentration: 70 mg L <sup>-1</sup> Adsorption time: 16 h
Adsorption kinetics	Adsorption time (min) 5, 10, 20, 40, 120, 240, 360, 960	Solution pH: 5.0 Adsorbent dose: 0.5 g L <sup>-1</sup> Initial TC concentration: 70 mg L <sup>-1</sup>
Adsorption isotherms	Initial TC concentration (C <sub>0</sub> , mg L <sup>-1</sup> ) 30, 50, 70, 110, 150, 200, 300, 350, 400	Solution pH: 5.0 Adsorbent dose: 0.5 g L <sup>-1</sup> Adsorption time: 16 h

<sup>a</sup> Adjusted by 0.1 M HCl and 0.1 M NaOH.

Each experiment included a blank control and three replicates, with the final equilibrium concentration determined as the average of the three replicates.

## 3 Results and discussion

### 3.1 Characterization

Fig. 1 illustrates the FTIR spectra of Gi, GO, Fe<sub>3</sub>O<sub>4</sub>, bio-cellulose, GO/Fe<sub>3</sub>O<sub>4</sub>/bio-cellulose aerogel before and after the TC adsorption, and TC in the wavenumber range of 500–4000 cm<sup>-1</sup>. In comparison to the FTIR spectrum of Gi, that of GO displayed a number of vibrational features at around 3200, 1730, 1630, 1380, 1220, and 1050 cm<sup>-1</sup>, representing the plentiful functional groups of O–H (hydroxyl) stretching, C=O (carbonyl) stretching, and C=C stretching in aromatic structure, C–O–H bending, C–O–C (epoxy) stretching, and C–O stretching vibrations, respectively.<sup>43,72–74</sup> The presence of the numerous oxygen-containing functionalities firmly proved that Gi was oxidized *via* the modified Hummers' method to produce GO. It is noticeable that both Gi and GO absorbed CO<sub>2</sub> at the vibrational peak of 2350 cm<sup>-1</sup>,<sup>75–77</sup> which also appeared in the FTIR spectra of the other samples. With respect to the FTIR spectrum of Fe<sub>3</sub>O<sub>4</sub>, a sharp and strong adsorption peak at 550 cm<sup>-1</sup> was assigned to Fe–O stretching vibration of Fe<sub>3</sub>O<sub>4</sub>.<sup>3,78</sup> This peak was also seen in the FTIR spectra of GO/Fe<sub>3</sub>O<sub>4</sub>/bio-cellulose aerogel, demonstrating the successful synthesis of Fe<sub>3</sub>O<sub>4</sub> and its integration in the composite aerogel. For the FTIR spectra of bio-cellulose, vibrational modes at the adsorption band around 3340 cm<sup>-1</sup> (O–H stretching) and the multiple intense peaks of 1160, 1107, and 1030 cm<sup>-1</sup> were attributed to C–O–C and C–O bonds in the structural skeleton of cellulose, confirming the fruitful preparation of cellulose from banana peels.<sup>2,69</sup> Additionally, the adsorption peak at approximately 2910 cm<sup>-1</sup> was associated with C–H stretching vibration in the –CH<sub>2</sub> group of cellulose.<sup>76,79</sup> It is noteworthy that these vibrations in the FTIR spectrum of bio-cellulose were also observed on the FTIR spectrum of the GO/Fe<sub>3</sub>O<sub>4</sub>/bio-cellulose aerogel but with less intensity owing to its lower content in comparison to the pristine bio-cellulose. Thus, all observations were combined to conclude the successful preparation of GO/Fe<sub>3</sub>O<sub>4</sub>/bio-cellulose aerogel.

Fig. 2a demonstrates the Raman spectra of Gi, GO, and GO/Fe<sub>3</sub>O<sub>4</sub>/bio-cellulose aerogel, while those of Fe<sub>3</sub>O<sub>4</sub> and bio-cellulose are displayed in Fig. 2b. Regarding carbonaceous materials in Fig. 2a, the G band at the Raman shift of 1592 cm<sup>-1</sup> represented the in-plane vibration of the sp<sup>2</sup>-hybridized carbon atoms in the aromatic structure, while the D band at the Raman shift of 1342 cm<sup>-1</sup> was assigned to the sp<sup>3</sup>-hybridized

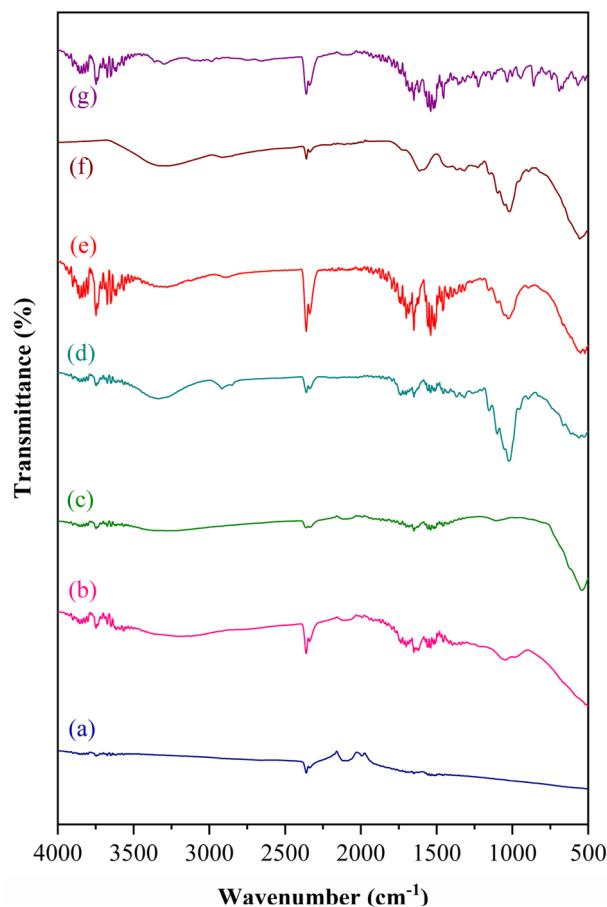


**Fig. 1** FTIR spectra of (a) Gi, (b) GO, (c) Fe<sub>3</sub>O<sub>4</sub>, (d) bio-cellulose, (e) GO/Fe<sub>3</sub>O<sub>4</sub>/bio-cellulose aerogel before the TC adsorption, (f) GO/Fe<sub>3</sub>O<sub>4</sub>/bio-cellulose aerogel after the TC adsorption, and (g) TC.





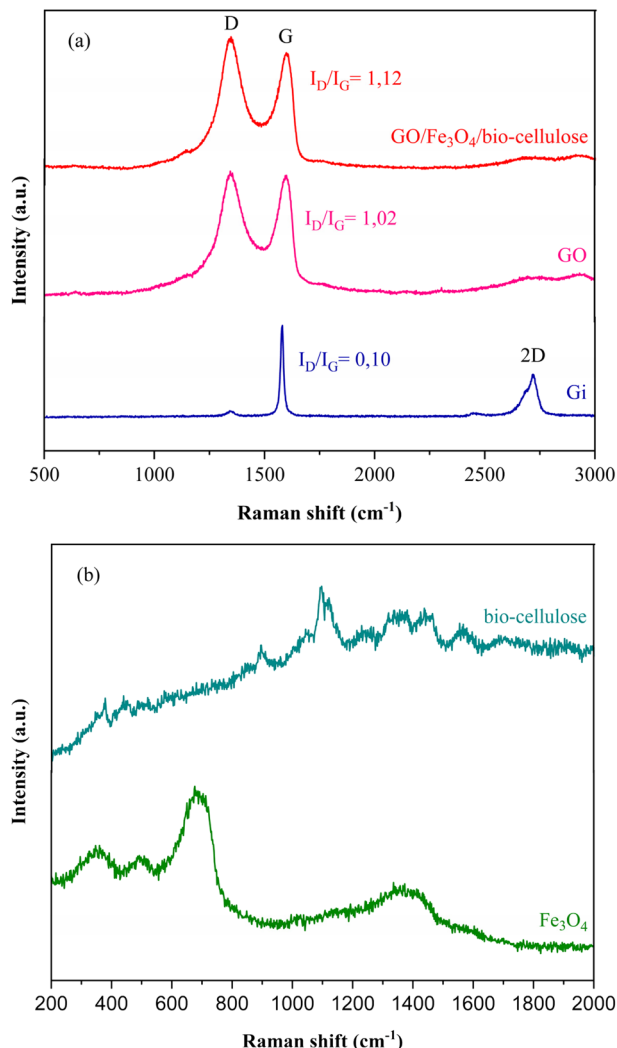


Fig. 2 Raman spectra of (a) Gi, GO, GO/Fe<sub>3</sub>O<sub>4</sub>/bio-cellulose aerogel and (b) Fe<sub>3</sub>O<sub>4</sub>, bio-cellulose.

counterparts in disordered behaviors.<sup>80,81</sup> The degree of defects could be determined *via* the intensity ratio of D band to G band ( $I_D/I_G$ ), meaning that more structural disorders were stated when seeing an increment in the ratio.<sup>55,82</sup> The  $I_D/I_G$  ratios of Gi and GO increased from 0.1 to 1.02, confirming that GO was obtained from Gi by the oxidation reactions. This ratio of GO/Fe<sub>3</sub>O<sub>4</sub>/bio-cellulose aerogel was 1.12, indicating that the GO in the composite aerogel had become more disordered.<sup>82</sup> From Fig. 2b, the Raman spectrum of Fe<sub>3</sub>O<sub>4</sub> was characterized at 683 cm<sup>-1</sup>, corresponding to the A<sub>1g</sub> mode of vibration, while the other peaks at 349 and 515 cm<sup>-1</sup> were assigned to the T<sub>2g</sub> mode of vibration.<sup>83–85</sup> With regard to the Raman spectrum of bio-cellulose, the peaks at the Raman shifts of 898, 1098, 1256, 1359, and 1570 cm<sup>-1</sup> were ascribed to the conformation of cellulose.<sup>86,87</sup> Consequently, the Raman spectra analysis emphasized the formation of GO, Fe<sub>3</sub>O<sub>4</sub>, bio-cellulose, and GO/Fe<sub>3</sub>O<sub>4</sub>/bio-cellulose, as aforementioned in the results of FTIR spectra.

The crystal structure of the synthesized materials was determined using XRD. Fig. 3 depicts the XRD patterns of Gi,

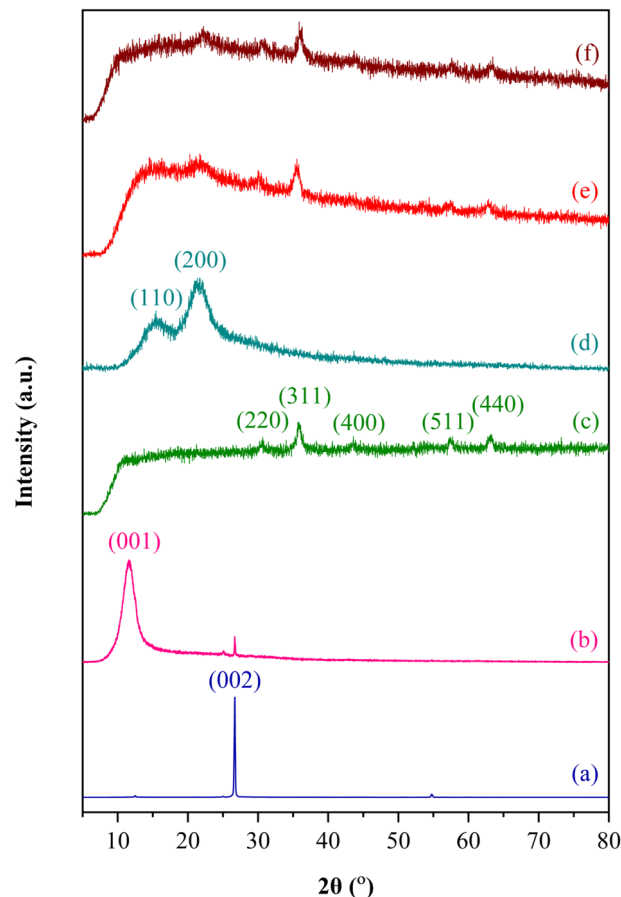


Fig. 3 XRD patterns of (a) Gi, (b) GO, (c) Fe<sub>3</sub>O<sub>4</sub>, (d) bio-cellulose, (e) GO/Fe<sub>3</sub>O<sub>4</sub>/bio-cellulose aerogel before the TC adsorption, and (f) GO/Fe<sub>3</sub>O<sub>4</sub>/bio-cellulose aerogel after the TC adsorption.

GO, Fe<sub>3</sub>O<sub>4</sub>, bio-cellulose, GO/Fe<sub>3</sub>O<sub>4</sub>/bio-cellulose aerogel before the TC adsorption, and GO/Fe<sub>3</sub>O<sub>4</sub>/bio-cellulose aerogel after the TC adsorption in the diffraction angle  $2\theta$  range of 5–80°. As can be seen, there was a translation from the characteristic diffraction peak of Gi at  $2\theta$  of 26.65° to that of GO at  $2\theta$  of 11.57°, corresponding to the change of (002) crystal plane into (001) crystal plane, respectively. This signified the formation of GO was obtained by the oxidation of Gi.<sup>80,88</sup> The XRD analysis of Fe<sub>3</sub>O<sub>4</sub> confirmed that diffraction peaks characterized at  $2\theta$  of 30.42°, 35.78°, 43.60°, 57.37°, and 62.96° were ascribed to (220), (311), (400), (511), and (440) crystal planes of Fe<sub>3</sub>O<sub>4</sub> nanoparticles,<sup>89–91</sup> which was in agreement with the literature of JCPDS no. 19-0629 for the standard XRD patterns of magnetite.<sup>85</sup> These peaks were also identified in the XRD pattern of the magnetic GO/Fe<sub>3</sub>O<sub>4</sub>/bio-cellulose aerogel, proving the incorporation of Fe<sub>3</sub>O<sub>4</sub> in the composite aerogel.<sup>3</sup> Regarding the XRD pattern of bio-cellulose, diffraction peaks anchored at  $2\theta$  of 15.34° and 21.93°, corresponding to (110) and (200) crystal planes, respectively, were characteristic peaks of cellulose.<sup>69,79</sup> These diffraction peaks of cellulose were found in the XRD pattern of the GO/Fe<sub>3</sub>O<sub>4</sub>/bio-cellulose aerogel but appeared more broadened compared to that of bio-cellulose, possibly signifying the its interaction with GO in the composite



aerogel.<sup>2,92</sup> The XRD results were consistent with the FTIR and Raman analyses to confirm the successful syntheses of GO, Fe<sub>3</sub>O<sub>4</sub>, bio-cellulose, and GO/Fe<sub>3</sub>O<sub>4</sub>/bio-cellulose aerogel.

The surface morphology of GO, Fe<sub>3</sub>O<sub>4</sub>, bio-cellulose, and GO/Fe<sub>3</sub>O<sub>4</sub>/bio-cellulose aerogel was monitored using FE-SEM (Fig. 4). The FE-SEM images of GO consisted of homogeneous thin layers with many wrinkles on the surface at both top view (Fig. 4b and h) and cross-section view (Fig. 4e), which is assumed to enlarge the surface area of GO sheets.<sup>55,93,94</sup> This also confirmed that graphite oxide was exfoliated by the sonication to produce the layers of GO.<sup>73,95</sup> For the FE-SEM images of bio-cellulose, it was witnessed as a stratified laminar structure of film-like layers on the top view (Fig. 4c) image or fiber-shaped bundles on the cross-section view counterpart (Fig. 4f), which could be due to the integration of cellulose nanofibers during preparation processes.<sup>96–98</sup> Fig. 4g showed the spherical shape of Fe<sub>3</sub>O<sub>4</sub> particles aggregated together because of their magnetic interactions.<sup>99</sup> For the FE-SEM images of GO/Fe<sub>3</sub>O<sub>4</sub>/bio-cellulose aerogel, the well-assembled and interconnected structure could be observed on the top view image (Fig. 4a), and especially on the cross-section view image (Fig. 4d). The blending of GO sheets with the skeletal structure of cellulose might strengthen the structure of the magnetic GO/Fe<sub>3</sub>O<sub>4</sub>/bio-cellulose composite aerogel.

EDX elemental mapping was employed to track the scattering of elements in the composite (Fig. 5). The intensities

associated with C, O, Fe, and Cl elements in the EDX spectrum were identified. Accordingly, C and O elements were anchored densely and uniformly throughout the surface of GO/Fe<sub>3</sub>O<sub>4</sub>/bio-cellulose aerogel, proving the abundance of the oxygen-containing functional groups. The existence of a negligible amount of Cl could be observed in the EDX spectrum, which was attributable to the use of NaClO during the bleaching treatment of bio-cellulose.<sup>100</sup> The EDX mapping of Fe revealed the highly dispersed Fe<sub>3</sub>O<sub>4</sub> attached to the aerogel, allowing the convenient separation of solid materials from aqueous media.

The specific surface areas of the GO, bio-cellulose, and GO/Fe<sub>3</sub>O<sub>4</sub>/bio-cellulose aerogel were determined using the BET method, yielding values of 40.1, 24.4, and 36.8 m<sup>2</sup> g<sup>−1</sup>, respectively. The obtained surface area of the composite aerogel in this study is similar to those of the hybrid GO/microcrystalline cellulose aerogel reported by Wei X. *et al.*<sup>101</sup> The intermediate value of the specific surface area of the composite aerogel compared to the components indicated the incorporation of bio-cellulose and GO sheets in the final product.

The magnetic property of GO/Fe<sub>3</sub>O<sub>4</sub>/bio-cellulose aerogel was compared with that of pristine Fe<sub>3</sub>O<sub>4</sub>. As shown in Fig. 6, the nearly zero values of magnetic remanence and coercivity of both hysteresis curves demonstrated their superparamagnetic property.<sup>102</sup> The saturation magnetization parameter (M<sub>s</sub>) of Fe<sub>3</sub>O<sub>4</sub> was 61.8 emu g<sup>−1</sup>, while that of the composite was 16.2 emu g<sup>−1</sup>. This lower saturation magnetization of the composite aerogel

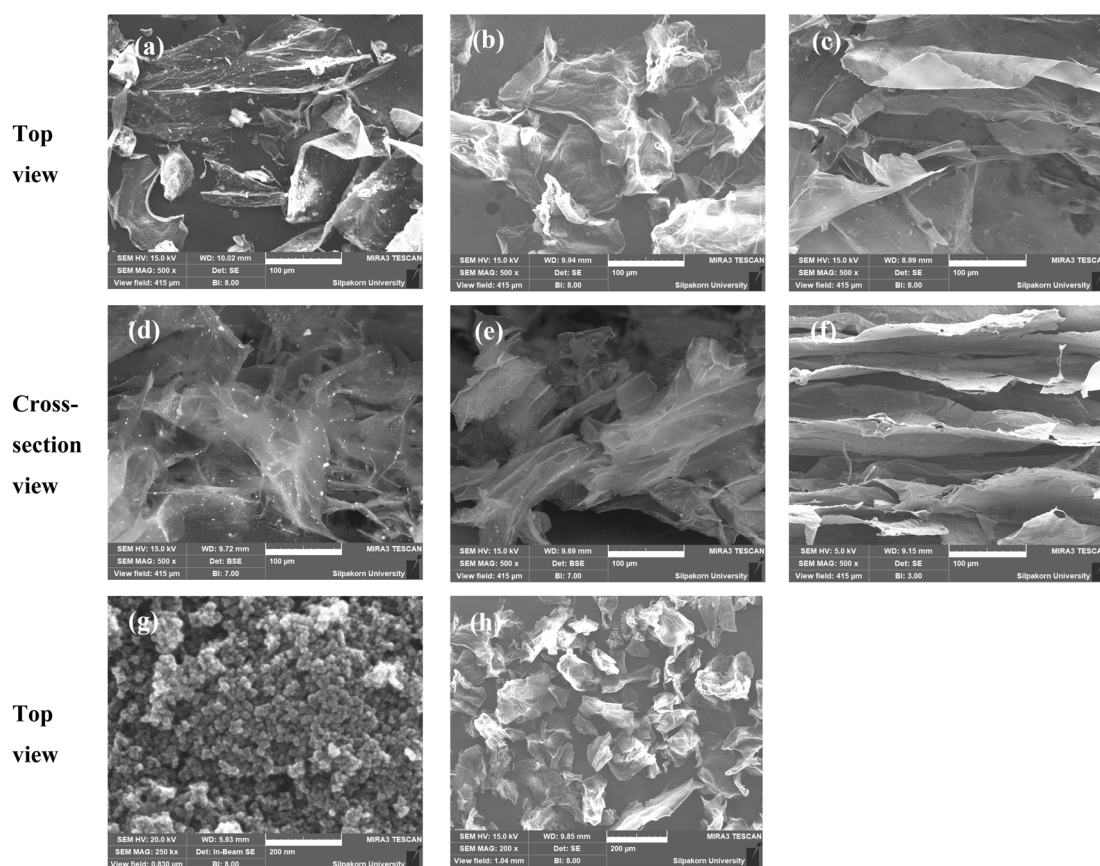


Fig. 4 FE-SEM top view images of (a) GO/Fe<sub>3</sub>O<sub>4</sub>/bio-cellulose aerogel, (b) and (h) GO, (c) bio-cellulose, (g) Fe<sub>3</sub>O<sub>4</sub>, and FE-SEM cross-section view images of (d) GO/Fe<sub>3</sub>O<sub>4</sub>/bio-cellulose aerogel, (e) GO, (f) bio-cellulose at different magnifications.



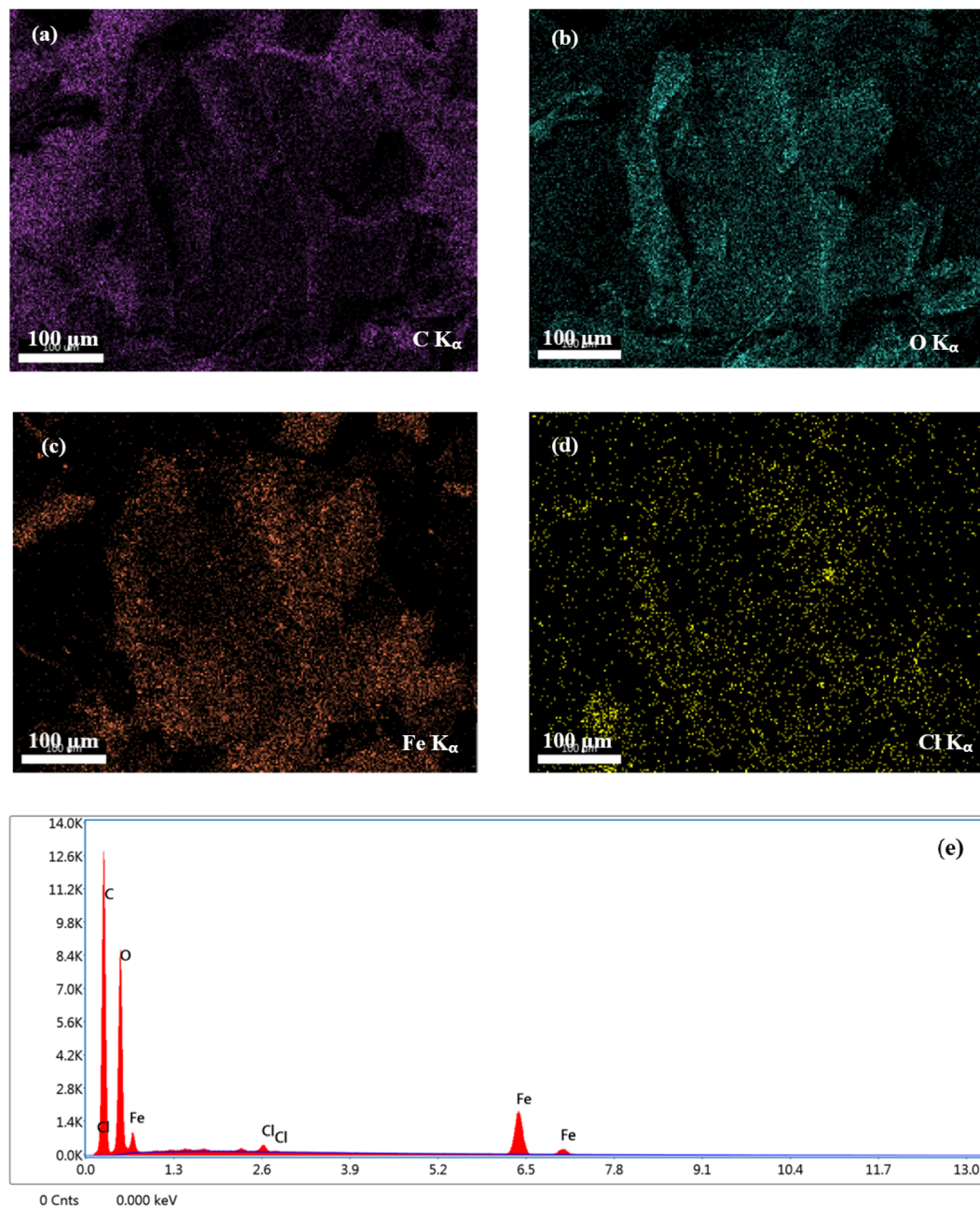


Fig. 5 Elemental mapping images of (a) C, (b) O, (c) Fe, and (d) Cl; (e) EDX spectrum of GO/Fe<sub>3</sub>O<sub>4</sub>/bio-cellulose aerogel.

could be attributed to the non-magnetic phases of GO or bio-cellulose, yet that value was strong enough to separate the aerogel after use.

### 3.2 Adsorption studies

**3.2.1 Effect of solution pH.** The ionization level of the surface functional groups of materials can be governed by adjusting the solution, consequently determining their adsorption capacity.<sup>103</sup> The speciation of TC is also dependent on solution pH since its pKa1, pKa2, and pKa3 values are 3.3, 7.7, and 9.7, respectively.<sup>104</sup> When the solution pH is between 3.3 and 7.7, TC exists as a zwitterionic species. At pH below 3.3,

TC predominates in a cationic form (TCH<sup>3+</sup>), while negatively charged species (TCH<sup>-</sup> and TC<sup>2-</sup>) are found when pH is above 7.7. In order to study the effect of the solution pH on the adsorption performance of the aerogel, the adsorption processes were carried out at the initial pH values ranging from 3.0 to 10.0. As illustrated in Fig. 7a, the adsorption performance of the aerogel in eliminating TC witnessed a remarkable improvement with the increment of pH from 2.0 to 5.0. It is noticeable that there was no statistically significant difference in the adsorption capacity of the aerogel at pH 5.0 and pH 6.0 (*t*-test, *P* = 0.23) with a 95% confidence interval ( $\alpha$  = 0.05). When the pH rose from 6.0 to 10.0, the adsorption capacity had a downward tendency. To elucidate these results, the



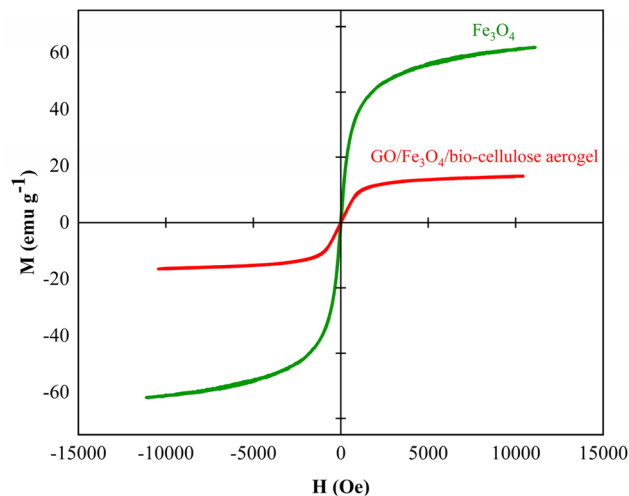


Fig. 6 Magnetization hysteresis curve of  $\text{Fe}_3\text{O}_4$  and the  $\text{GO}/\text{Fe}_3\text{O}_4/\text{bio-cellulose}$  aerogel.

determination of the  $\text{pH}_{\text{pzc}}$  of the aerogel was conducted, revealing the  $\text{pH}_{\text{pzc}}$  value of 3.5 (Fig. 7b). This finding indicates that the surface of the aerogel was negatively charged at pH over 3.5 and positively charged at pH below 3.5. The effect of solution pH on adsorption capacity could be then ascribed to the electrostatic interaction between the charged surface of the aerogel and different forms of TC. At pH below 3.5, the electrostatic repulsion between the cationic form of TC and positively charged aerogel caused the low adsorption capacity. When the pH reached 5.0, TC transferred to the zwitterionic form ( $\text{TCH}_2^\pm$ ).<sup>104</sup> The electrostatic attraction between the positive charge of TC and the negative charge of the aerogel surface turned out to be preferable, thereby enhancing the adsorption capacity. It is worth noting that the zwitterion existed at maximum concentration in the pH range of 5.0–6.0,<sup>104</sup> leading to the highest adsorption capacity of TC at this pH range. When the pH increased from 6.0 to 10.0, the formation of anionic TC ( $\text{TCH}^-$  and  $\text{TC}^{2-}$ ) promoted the electrostatic repulsion between these anions and the negatively charged surface of the aerogel. As a result, a reduction in the adsorption capacity was attained. From all the results, the initial pH of 5.0 was selected for subsequent adsorption experiments.

**3.2.2 Effect of adsorbent dose.** Fig. 8 displays the effect of the adsorbent dose on the removal of TC. It can be observed that the adsorption capacity of the aerogel showed a drastic decline from the peak value of  $101.6 \pm 2.6 \text{ mg g}^{-1}$  at a dose of  $0.50 \text{ g L}^{-1}$  to the bottom of  $51.7 \pm 0.02 \text{ mg g}^{-1}$  at a dose of  $1.33 \text{ g L}^{-1}$ . These results could be assigned to the agglomeration of the materials at high doses, resulting in a significant obstruction of available active sites.<sup>105–107</sup> Notably, the noteworthy adsorption capacity at a low adsorbent dose demonstrated the promising adsorption performance of the aerogel in far-reaching applications. This not only lowers the cost of adsorption but also mitigates the risk of secondary pollution associated with the excess use of adsorbent in the treatment process.<sup>108</sup> Therefore, the adsorbent dose for the TC removal was established at  $0.5 \text{ g L}^{-1}$  for further experiments.

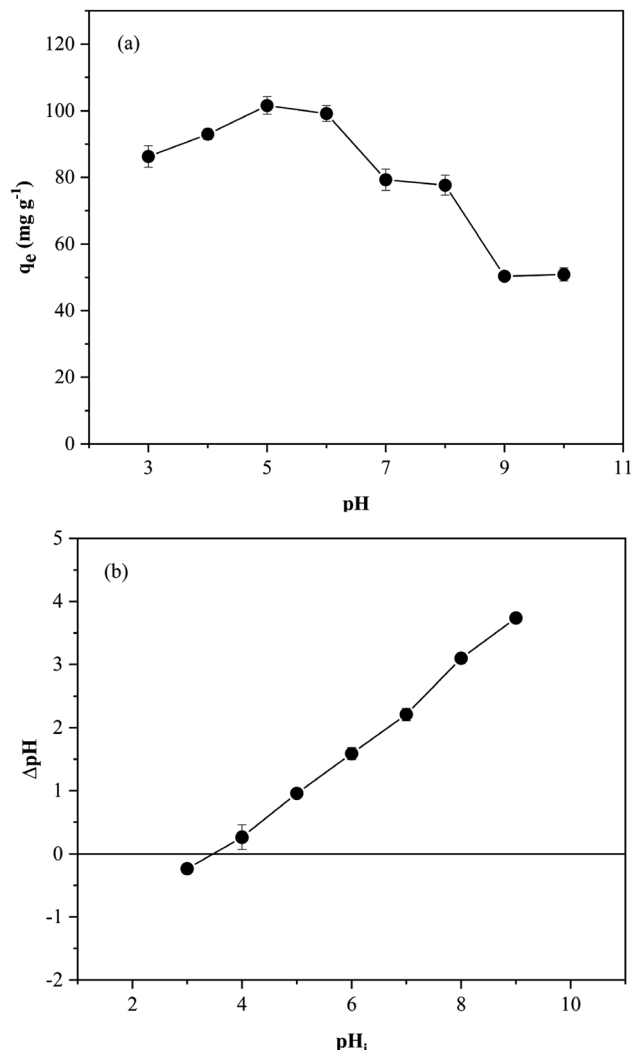


Fig. 7 (a) Effect of pH on TC adsorption, and (b) point of zero charge of  $\text{GO}/\text{Fe}_3\text{O}_4/\text{bio-cellulose}$  aerogel.

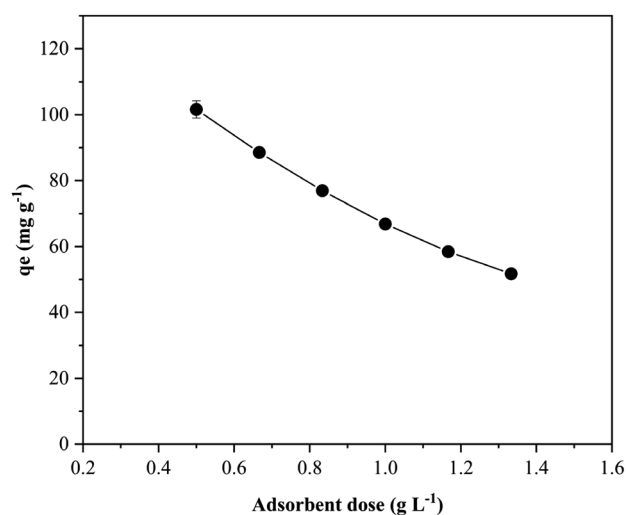


Fig. 8 Effect of the adsorbent dose on TC adsorption capacity.





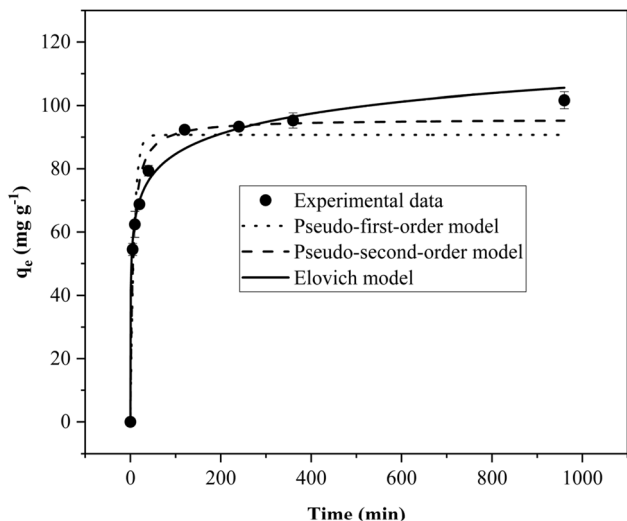


Fig. 9 Non-linear kinetic models for the TC adsorption onto the GO/Fe<sub>3</sub>O<sub>4</sub>/bio-cellulose aerogel.

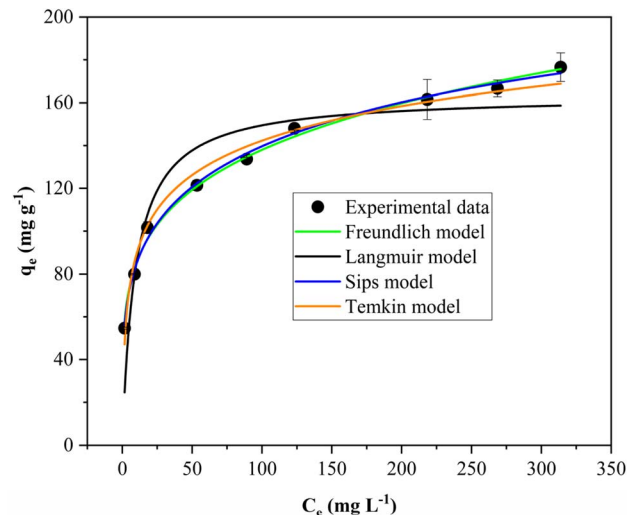


Fig. 10 Non-linear isotherm plots for the TC adsorption onto the GO/Fe<sub>3</sub>O<sub>4</sub>/bio-cellulose aerogel.

**3.2.3 Adsorption kinetics.** The investigation of adsorption kinetics of a specific adsorbent/adsorbate system is necessary to provide the information of kinetic parameters for the design of adsorption processes on studied materials.<sup>105,109</sup> The adsorption of the aerogel was therefore carried out at different contact times, ranging from 5 to 960 min. As depicted in Fig. 9, the adsorption capacity increased significantly with the extension of contact time from 5 to 120 min and followed by a slower increase between 120 and 960 min. The experimental data were subsequently examined through three distinct non-linear kinetic models, encompassing the pseudo-first-order, pseudo-second-order, and Elovich.<sup>110–112</sup> The equations and non-linear graphs for each model are detailed in Table 2 and illustrated in Fig. 9, respectively. The corresponding parameters are also presented in Table 2. The experimental kinetic data in this study displayed the best fit with the Elovich model, with the highest regression coefficient ( $R^2 = 0.991$ ). The initial rate of the adsorption process determined by this model was found to be  $0.89 \text{ g g}^{-1} \text{ min}^{-1}$ . After the initial stage with a high adsorption rate, the rate decreased over time due to an increase in occupied surface sites.<sup>113,114</sup> This is contributed by the assumption of the model that the adsorption process occurs on the heterogeneous

surfaces of materials where different surface sites have different adsorption energies.<sup>112,113</sup> The surface heterogeneity is intrinsic to composite materials like the magnetic GO/Fe<sub>3</sub>O<sub>4</sub>/bio-cellulose composite aerogel in this study, which consists of different components possessing different chemical functionalities and surface characteristics. The organic pollutant tended to be quickly adsorbed on favorable sites or high-energy sites, leading to a rapid adsorption rate. The remaining low-energy sites were then occupied, which slowed down the adsorption rate over time.

**3.2.4 Adsorption isotherms.** The equilibrium performance of the adsorbents was investigated by carrying out the adsorption isotherm experiments. Four popular non-linear isotherm models, including Langmuir,<sup>115</sup> Freundlich,<sup>116</sup> Sips,<sup>117</sup> and Temkin,<sup>118</sup> were used to analyze the experimental equilibrium data. The impact of the initial TC concentration on the adsorption capacity, along with the non-linear graphs of the three adsorption isotherm models, are illustrated in Fig. 10. As the initial TC concentration increased, the adsorption capacity also showed an enhancement. The equations of the studied models and the calculated parameters are provided in Table 3. Based on the correlation coefficient ( $R^2$ ) values, it is clear that

Table 2 Kinetic parameters for the TC adsorption onto the GO/Fe<sub>3</sub>O<sub>4</sub>/bio-cellulose aerogel<sup>a</sup>

Kinetic models and corresponding equations	Kinetic model parameters and regression coefficients		
Pseudo-first-order	$k_1 \text{ (min}^{-1}\text{)}$	$q_e \text{ (mg g}^{-1}\text{)}$	$R^2$
$q_t = q_e (1 - \exp(-k_1 t))$	0.12	90.7	0.920
Pseudo-second-order	$k_2 \text{ (g mg}^{-1} \text{ min}^{-1}\text{)}$	$q_e \text{ (mg g}^{-1}\text{)}$	$R^2$
$q_t = \frac{q_e^2 k_2 t}{q_e k_2 t + 1}$	0.002	95.7	0.977
Elovich	$\alpha \text{ (g g}^{-1} \text{ min}^{-1}\text{)}$	$\beta \text{ (g mg}^{-1}\text{)}$	$R^2$
$q_t = \frac{1}{\beta} \ln(1 + \alpha \beta t)$	0.89	0.11	0.991

<sup>a</sup>  $q_e/q_t \text{ (mg g}^{-1}\text{)}$ : adsorption capacity at equilibrium/at time  $t$ ;  $k_1 \text{ (min}^{-1}\text{)}/k_2 \text{ (g mg}^{-1} \text{ min}^{-1}\text{)}$ : the respective rate constants of kinetics models;  $\alpha \text{ (g g}^{-1} \text{ min}^{-1}\text{)}$ : initial sorption rate of the Elovich model;  $\beta \text{ (g mg}^{-1}\text{)}$ : the Elovich constant.



Table 3 Isotherm parameters for the TC adsorption onto the GO/Fe<sub>3</sub>O<sub>4</sub>/bio-cellulose aerogel<sup>a</sup>

Isotherm models and corresponding equations		Adsorption isotherm model parameters		
Freundlich		$K_F$ (mg g <sup>-1</sup> )	$1/n_F$	$R^2$
$q_e = K_F C_e^{1/n}$		52.3	0.21	0.994
Langmuir	$q_m$ (mg g <sup>-1</sup> )	$K_L$ (L mg <sup>-1</sup> )		$R^2$
$q_e = \frac{q_m K_L C_e}{1 + K_L C_e}$	163.4	0.11		0.863
Sips	$q_m$ (mg g <sup>-1</sup> )	$b_s$ (mg <sup>-1/n</sup> L <sup>-1/n</sup> )	$n_s$	$R^2$
$q_e = \frac{q_m (b_s C_e)^n}{1 + (b_s C_e)^n}$	238.7	0.001	0.23	0.995
Temkin		$b_T$ (kJ mol <sup>-1</sup> )	$A_T$ (L mg <sup>-1</sup> )	$R^2$
$q_e = \frac{RT}{b_T} \ln(A_T C_e)$		0.11	4.6	0.983

<sup>a</sup>  $q_e$ : equilibrium adsorption capacity;  $n_F$ : the Freundlich constant;  $C_e$ : equilibrium concentration of adsorbate;  $K_F$ : a Freundlich constant related to adsorption capacity;  $q_m$ : maximum adsorption capacity of adsorbent;  $K_L$ : Langmuir constant related to energy of adsorption;  $b_s$ : Sips constant;  $n_s$ : the heterogeneity factor;  $b_T$ : Temkin constant;  $A_T$ : Temkin isotherm constant.

the Sips and Freundlich were the most appropriate models for the experimental data. The Freundlich model describes multi-layer adsorption that happens with heat and affinities scattering over a heterogeneous surface.<sup>119,120</sup> The Freundlich constant ( $1/n$ ) represents the adsorption intensity, heterogeneity factor, and the heterogeneity of site energies.<sup>120,121</sup> According to Tseng *et al.*,<sup>121</sup> the favorable adsorption level can be inferred by this constant (Table 4). The  $1/n$  value obtained in this study was found to be 0.21, indicating the favorable adsorption of TC on the heterogeneous surface of the desired GO/Fe<sub>3</sub>O<sub>4</sub>/bio-cellulose aerogel. The Sips isotherm model is a combination of Freundlich and Langmuir expressions.<sup>122</sup> The Sips constant ( $n$ ) represents the degree of surface heterogeneity of adsorbents and characteristics of adsorption processes. When  $n$  reaches 1, the Sips model reduces to Langmuir isotherm model with the assumption of monolayer adsorption on a homogeneous surface.<sup>123</sup> On the other hand, it resembles the Freundlich isotherm model when  $n$  deviates from 1, which accounts for the adsorption on heterogeneous surface with different adsorption site energies. In this study, it can be observed that the Sips constant ( $n = 0.23$ ) is much lower than 1, which is Freundlich-like behavior.<sup>123</sup> This is in good agreement with the findings when fitting experiment data with individual Langmuir and Freundlich models. Moreover, it is worth mentioning that the findings from the study of adsorption isotherm were consistent with those from the adsorption kinetics, confirming that the adsorption of TC occurred on the heterogeneous surface of GO/Fe<sub>3</sub>O<sub>4</sub>/bio-cellulose composite aerogel with a wide distribution of adsorption site energies.

Table 4 Freundlich favorable parameters<sup>121</sup>

$1/n$	Favorable level
$1/n < 0.01$	Pseudo-irreversible
$0.01 < 1/n < 0.1$	Strong favorable
$0.1 < 1/n < 0.5$	Favorable
$0.5 < 1/n < 1$	Pseudo-linear
$1/n = 1$	Linear
$1/n > 1$	Unfavorable

The maximum adsorption capacity obtained from the Sips isotherm model in this study was compared to other similar reported adsorbents (Table 5). It is apparent that the synthesized composite aerogel offers a comparable adsorption capacity to other adsorbents previously reported. Considering that banana peels are one of the most abundant agro-wastes worldwide, there is a great possibility of developing potentially valuable material derived from this agricultural waste for the removal of antibiotics from aqueous media. Furthermore, the composite aerogel obtained in this study offers the advantage of a convenient separation using external magnetic fields.

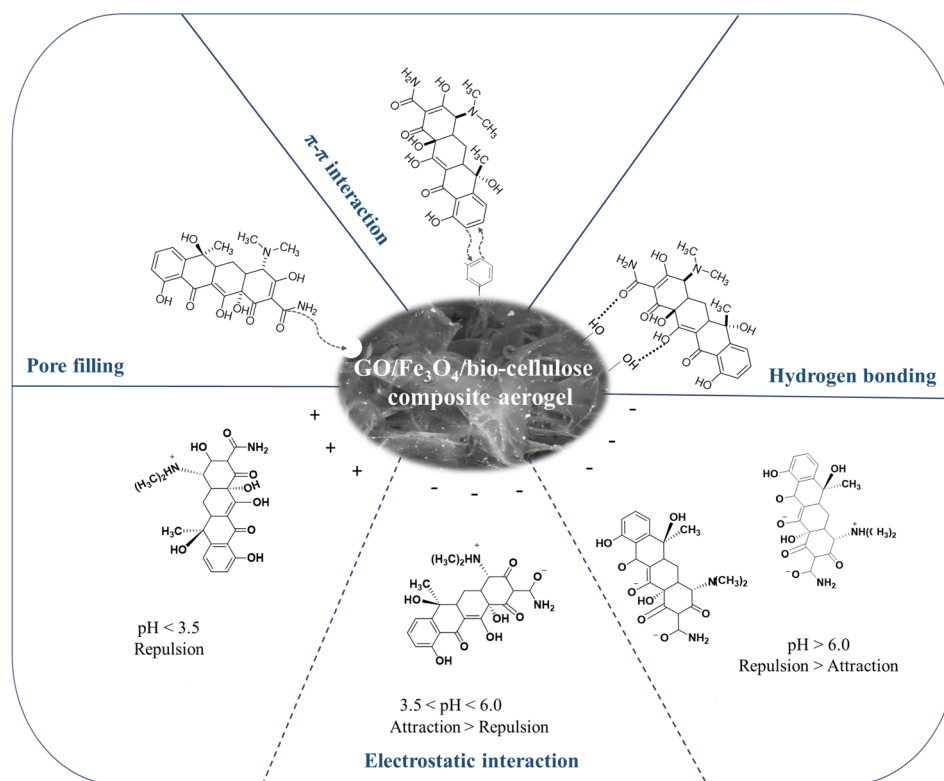
**3.2.5 Adsorption mechanism.** To study the adsorption mechanism, the FTIR spectrum and XRD pattern of the GO/Fe<sub>3</sub>O<sub>4</sub>/bio-cellulose aerogel after being used for the TC adsorption were measured and presented in Fig. 1f and 3f, respectively. With respect to the XRD patterns in Fig. 3, the XRD pattern of the aerogel after being used was similar to that of the original aerogel, indicating the crystalline structure of the aerogel was maintained during the adsorption process. This implied that the adsorption occurred on the surface or within the porous structure of the aerogel. As shown from the FTIR spectrum of TC in Fig. 1g, the adsorption peaks at around 3300 cm<sup>-1</sup> (O-H), 1654 cm<sup>-1</sup> (C=O), 1620 cm<sup>-1</sup> (N-H primary amine), 1530 cm<sup>-1</sup> (C=C), 1450 cm<sup>-1</sup> (C-N), 1350 cm<sup>-1</sup> (C-O in the amide group), and 1030 cm<sup>-1</sup> (NH<sub>2</sub> amino group) were assigned to the vibrational features of TC.<sup>129-132</sup> In comparison to the FTIR spectra of the GO/Fe<sub>3</sub>O<sub>4</sub>/bio-cellulose aerogel before the TC adsorption, the presence of the additional vibrations around 1620, 1450, and 1350 cm<sup>-1</sup> in that of the aerogel after the TC adsorption could be ascribed to the existence of TC. This confirmed that TC was adsorbed by the GO/Fe<sub>3</sub>O<sub>4</sub>/bio-cellulose aerogel. Moreover, it is worth noting that a translation was observed in the absorption band of aromatic C=C of the aerogel before (1630 cm<sup>-1</sup>) and after (1595 cm<sup>-1</sup>) the adsorption process. This could deduce that the aromatic C=C with  $\pi$  electrons of TC could create  $\pi$ - $\pi$  interactions with the aromatic rings in the aerogel.<sup>130</sup>

In addition to FTIR and XRD characterizations, based on the results obtained regarding the effect of the solution pH, the



**Table 5** Comparison of maximum adsorption capacity ( $q_m$ ) according to the Sips isotherm model for tetracycline removal using bio-based adsorbent

Biochar-based adsorbents	$q_m$ (mg g <sup>-1</sup> )	Reference
Fe <sub>3</sub> O <sub>4</sub> /coffee residue composite	179.85	124
Iron- and nitrogen-modified walnut shell-based biochar	238.94	125
Sludge-bamboo biochar	122.68 (308 K)	126
Graphene oxide loaded with titanium dioxide composites	173.44	127
Magnetic graphene oxide nanocomposite modified with polyvinylpyrrolidone	193.8 (308 K)	128
Magnetic graphene oxide/Fe <sub>3</sub> O <sub>4</sub> /banana peel-derived cellulose composite aerogels	238.7	This study

**Fig. 11** Proposed mechanism of the TC adsorption onto the GO/Fe<sub>3</sub>O<sub>4</sub>/bio-cellulose aerogel.

adsorption was found to be preferable at the solution pH that promoted the electrostatic attraction between the charged site of TC and the charged surface of the aerogel. Hence, the major mechanism proposed in this study is electrostatic interactions. It is worth noting that the TC removal also took place at low pH values, which advocated the electrostatic repulsion despite low adsorption performance. Therefore, there was a potential for TC to interact with the aerogel through the pore-filling effect. Additionally, hydrogen bonds are associated with the origin of numerous physicochemical properties of compounds containing N and O elements.<sup>133,134</sup> From all the results collected from this study, a proposed adsorption mechanism of TC onto the magnetic GO/Fe<sub>3</sub>O<sub>4</sub>/bio-cellulose aerogels is depicted in Fig. 11. Potential interactions may involve the electrostatic interactions, hydrogen bonds, the pore-filling effects, and  $\pi$ - $\pi$  interactions between the magnetic GO/Fe<sub>3</sub>O<sub>4</sub>/bio-cellulose aerogel and TC.

## 4 Conclusions

The characterization results demonstrate that the magnetic GO/Fe<sub>3</sub>O<sub>4</sub>/bio-cellulose aerogel was successfully synthesized using the ultrasound-assisted mechanical mixing method and freeze-drying technique. Remarkably, the aerogel could be simply prepared using cellulose isolated from abundant banana peels and GO, with the aim of promoting adsorption performance. The VSM findings confirmed the magnetism of the aerogels, paving the way for convenient separation of the material from aqueous media after the adsorption experiments. The effects of solution pH and adsorbent dose on the adsorption capacity, along with the comprehensive elaborations of adsorption kinetics, isotherms, and mechanisms, were thoroughly elucidated in this study. The adsorption studies proved the promising potential of the magnetic GO/Fe<sub>3</sub>O<sub>4</sub>/bio-cellulose aerogel for TC removal. Subsequent studies focusing on the treatment



of practical antibiotics-containing wastewater will probably be essential to completely assess the adsorption performance of the magnetic GO/Fe<sub>3</sub>O<sub>4</sub>/bio-cellulose composite aerogel.

## Data availability

The data used to support the findings of this study are included within the manuscript.

## Conflicts of interest

The authors declare that there are no competing interests that could have appeared to influence the work reported in this paper.

## Acknowledgements

The authors declare that no funds or grants were received during the preparation of this manuscript.

## References

- N. C. Joshi and P. Gururani, *Curr. Res. Green Sustainable Chem.*, 2022, **5**, 100306.
- P. Joshi, O. P. Sharma, S. K. Ganguly, M. Srivastava and O. P. Khatri, *J. Colloid Interface Sci.*, 2022, **608**, 2870–2883.
- A. Dang, Y. Wang, Y. Liu, T. Cheng, A. Zada, F. Ye, W. Deng, Y. Sun, T. Zhao and T. Li, *J. Hazard. Mater.*, 2023, **457**, 131846.
- L. Zhang, X. Li, S. Chen, J. Guan, Y. Guo and W. Yu, *Catal. Commun.*, 2023, **176**, 106627.
- N. Baig, M. Sajid and T. A. Saleh, *J. Environ. Manage.*, 2019, **244**, 370–382.
- F. Wei, Q. Ren, H. Zhang, L. Yang, H. Chen, Z. Liang and D. Chen, *RSC Adv.*, 2021, **11**, 9977–9984.
- Y. Kong, Y. Zhuang, K. Han and B. Shi, *Colloids Surf., A*, 2020, **588**, 124360.
- Y. Zhao, Q. E. Yang, X. Zhou, F.-H. Wang, J. Muurinen, M. P. Virta, K. K. Brandt and Y.-G. Zhu, *Crit. Rev. Environ. Sci. Technol.*, 2021, **51**, 2159–2196.
- M. Beiranvand, S. Farhadi and A. Mohammadi-Gholami, *RSC Adv.*, 2022, **12**, 34438–34453.
- G. Gopal, S. A. Alex, N. Chandrasekaran and A. Mukherjee, *RSC Adv.*, 2020, **10**, 27081–27095.
- L. Xu, H. Zhang, P. Xiong, Q. Zhu, C. Liao and G. Jiang, *Sci. Total Environ.*, 2021, **753**, 141975.
- Y. Dai, M. Liu, J. Li, S. Yang, Y. Sun, Q. Sun, W. Wang, L. Lu, K. Zhang and J. Xu, *Sep. Sci. Technol.*, 2020, **55**, 1005–1021.
- Q. Liao, H. Rong, M. Zhao, H. Luo, Z. Chu and R. Wang, *Sci. Total Environ.*, 2021, **757**, 143981.
- J. Leichtweis, Y. Vieira, N. Welter, S. Silvestri, G. L. Dotto and E. Carissimi, *Process Saf. Environ. Prot.*, 2022, **160**, 25–40.
- A. Balakrishnan, M. Chinthala, R. K. Polagani and D.-V. N. Vo, *Environ. Res.*, 2023, **216**, 114660.
- M. Minale, Z. Gu, A. Guadie, D. M. Kabtamu, Y. Li and X. Wang, *J. Environ. Manage.*, 2020, **276**, 111310.
- C. Zhao, J. Ma, Z. Li, H. Xia, H. Liu and Y. Yang, *RSC Adv.*, 2020, **10**, 5066–5076.
- J. Li, J. Tao, C. Ma, J. Yang, T. Gu and J. Liu, *RSC Adv.*, 2020, **10**, 42038–42053.
- D. Morales-Serrato, J. Torres-Pérez, Á. de Jesús Ruiz-Baltazar and S. Y. Reyes-López, *Int. J. Res. GRANTHAALAYAH*, 2021, **9**, 446–491.
- O. A. Ajala, S. O. Akinshaw, A. Bamsaye, D. T. Adedipe, M. O. Adesina, O. A. Okon-Akan, T. A. Adebuseyi, A. T. Ojedokun, K. A. Adegoke and O. S. Bello, *RSC Adv.*, 2023, **13**, 4678–4712.
- M. A. Islam, B. Hameed, M. Ahmed, W. Khanday, M. A. Khan and F. Marrakchi, *Biomass Convers. Biorefin.*, 2023, **13**, 13153–13162.
- J. Yang, Y. Dou, H. Yang and D. Wang, *Appl. Surf. Sci.*, 2021, **538**, 148110.
- P. T. T. Ninh, N. D. Dat, M. L. Nguyen, N. T. Dong, H.-P. Chao and H. N. Tran, *Environ. Res.*, 2023, **218**, 114927.
- J. Miao, F. Wang, Y. Chen, Y. Zhu, Y. Zhou and S. Zhang, *Appl. Surf. Sci.*, 2019, **475**, 549–558.
- J. W. P. Lye, N. Saman, A. M. M. Noor, S. S. Mohtar, N. S. Othman, S. S. N. Sharuddin, H. Kong and H. Mat, *Chem. Eng. Technol.*, 2020, **43**, 1285–1296.
- S. Al-Salihi, M. M. Fidalgo and Y. Xing, *ACS ES&T Water*, 2023, **3**, 838–847.
- F. K. Mostafapour, M. Yilmaz, A. H. Mahvi, A. Younesi, F. Ganji and D. Balarak, *Desalin. Water Treat.*, 2022, **247**, 216–228.
- G. Yang, Q. Gao, S. Yang, S. Yin, X. Cai, X. Yu, S. Zhang and Y. Fang, *Chemosphere*, 2020, **239**, 124831.
- M. Foroughi, M. H. A. Azghandi and S. Kakhki, *J. Hazard. Mater.*, 2020, **388**, 121769.
- L. Vazirova and G. Abbasova, *Adv. Sci. Technol.*, 2024, **148**, 13–19.
- A. Maged, J. Iqbal, S. Kharbush, I. S. Ismael and A. Bhatnagar, *J. Hazard. Mater.*, 2020, **384**, 121320.
- J. Shang, M. Huang, L. Zhao, P. He, Y. Liu, H. Pan, S. Cao and X. Liu, *ACS Omega*, 2023, **9**, 692–699.
- M. I. Al-Wabel, M. Ahmad, A. R. Usman, A. S. Sallam, Q. Hussain, R. B. Binyameen, M. R. Shehu and Y. S. Ok, *J. Hazard. Mater.*, 2020, **384**, 121500.
- W. Wang, Z. Zhu, M. Zhang, S. Wang and C. Qu, *J. Taiwan Inst. Chem. Eng.*, 2020, **106**, 130–137.
- Y. Zhu, J. Shen, M. Guo, H. Zheng and Y. Cao, *Environ. Sci. Pollut. Res.*, 2023, **30**, 27315–27327.
- S. K. Sharma, P. Ranjani, H. Mamane and R. Kumar, *Sci. Rep.*, 2023, **13**, 16448.
- E. Tao, D. Ma, S. Yang and X. Hao, *J. Alloys Compd.*, 2020, **832**, 154833.
- P. Joshi, A. Raturi, M. Srivastava and O. P. Khatri, *J. Environ. Chem. Eng.*, 2022, **10**, 108597.
- A. K. Geim and K. S. Novoselov, *Nat. Mater.*, 2007, **6**, 183–191.
- M. S. Iqbal, A. A. Aslam, R. Iftikhar, M. Junaid, S. M. Imran, M. S. Nazir, Z. Ali, M. Zafar, A. Kanwal and N. K. Othman, *J. Water Process Eng.*, 2023, **53**, 103809.





- 41 D. R. Rout, H. M. Jena, O. Baigenzhenov and A. Hosseini-Bandegharraei, *Sci. Total Environ.*, 2023, **863**, 160871.
- 42 N. H. Dang, T. H. Tu, V. N. P. Linh, L. T. M. Thy, H. M. Nam, M. T. Phong and N. H. Hieu, *Synth. Met.*, 2019, **255**, 116106.
- 43 X. Hao, S. Yang, E. Tao, L. Liu, D. Ma and Y. Li, *J. Alloys Compd.*, 2022, **923**, 166335.
- 44 H. Zhang, X. Liu, B. Wang, Z. Shi, Z. Wei, Z. Wu, Y. Zhu, Q. Guo and X. Wang, *Chem. Eng. J.*, 2023, **465**, 142943.
- 45 Q. Wu, W. Wu, X. Zhan and X. Hou, *New J. Chem.*, 2020, **44**, 10654–10661.
- 46 D. B. Thinh, T. H. Tu, N. M. Dat, T. T. Hong, P. T. N. Cam, D. N. Trinh, H. M. Nam, M. T. Phong and N. H. Hieu, *Surf. Interfaces*, 2021, **26**, 101309.
- 47 L. Lentz, D. A. Mayer, M. Dogenski and S. R. S. Ferreira, *Mater. Chem. Phys.*, 2022, **283**, 125981.
- 48 A. Masud, C. Zhou and N. Aich, *Environ. Sci.: Nano*, 2021, **8**, 399–414.
- 49 J.-b. Huo, G. Yu and J. Wang, *Chemosphere*, 2021, **278**, 130492.
- 50 Y. He, C. Yi, X. Zhang, W. Zhao and D. Yu, *TrAC, Trends Anal. Chem.*, 2021, **136**, 116191.
- 51 D. Qiao, Z. Li, J. Duan and X. He, *Chem. Eng. J.*, 2020, **400**, 125952.
- 52 N. Shah, T. Rehan, X. Li, H. Tetik, G. Yang, K. Zhao and D. Lin, *RSC Adv.*, 2021, **11**, 7187–7204.
- 53 P. M. Tu, T. H. Lin, T. Q. Thang, D. N. C. Vy, C. V. Lam, N. T. Son, M. T. Phong and N. H. Hieu, *J. Mol. Struct.*, 2023, **1287**, 135737.
- 54 V. T. Nguyen, L. Q. Ha, L. C. T. Van, P. T. B. Huynh, D. M. Nguyen, V. P. Nguyen, T. H. Tran and D. Hoang, *J. Environ. Chem. Eng.*, 2023, **11**, 109523.
- 55 H. Dan, N. Li, X. Xu, Y. Gao, Y. Huang, M. Akram, W. Yin, B. Gao and Q. Yue, *Sci. Total Environ.*, 2020, **739**, 139983.
- 56 C. Ji, S. Yang, E. Tao, Y. Cheng, X. Hao and Y. Li, *J. Environ. Chem. Eng.*, 2021, **9**, 106819.
- 57 T. T. P. N. X. Trinh, T. H. Quan, T. N. M. Anh, D. B. Thinh, N. T. Lan, D. N. Trinh, N. M. Dat, H. M. Nam, M. T. Phong and N. H. Hieu, *Surf. Interfaces*, 2021, **23**, 101023.
- 58 B. El Allaoui, H. Benzeid, N. Zari and R. Bouhfid, *J. Drug Delivery Sci. Technol.*, 2023, 104899.
- 59 H. Seddiqi, E. Oliaei, H. Honarkar, J. Jin, L. C. Geonzon, R. G. Bacabac and J. Klein-Nulend, *Cellulose*, 2021, **28**, 1893–1931.
- 60 S. S. Jayan, J. S. Jayan and A. Saritha, *Int. J. Biol. Macromol.*, 2023, 125928.
- 61 A. H. Hashem, E. Saied and M. S. Hasanin, *Sustainable Chem. Pharm.*, 2020, **18**, 100333.
- 62 S. Mishra, P. S. Kharkar and A. M. Pethe, *Carbohydr. Polym.*, 2019, **207**, 418–427.
- 63 B. Yu, X. Zeng, L. Wang and J. M. Regenstein, *Carbohydr. Polym.*, 2021, **254**, 117415.
- 64 B. Ameha, T. T. Nadew, T. S. Tedla, B. Getye, D. A. Mengie and S. Ayalneh, *RSC Adv.*, 2024, **14**, 3675–3690.
- 65 V. S. Munagapati, J.-C. Wen, C.-L. Pan, Y. Gutha, J.-H. Wen and G. M. Reddy, *Int. J. Phytorem.*, 2020, **22**, 267–278.
- 66 M. Imran, A. Islam, M. U. Farooq, J. Ye and P. Zhang, *Environ. Sci. Pollut. Res.*, 2020, **27**, 43493–43504.
- 67 N. Zaaba, K. Foo, U. Hashim, S. Tan, W.-W. Liu and C. Voon, *Procedia Eng.*, 2017, **184**, 469–477.
- 68 T. T. T. Le Hoang, F. Unob, S. Suvokhiaw and N. Sukpirom, *J. Environ. Chem. Eng.*, 2020, **8**, 103653.
- 69 S. Mishra, B. Prabhakar, P. S. Kharkar and A. M. Pethe, *ACS Omega*, 2022, **8**, 1140–1145.
- 70 L.-T.-T.-T. Hoang, H.-V.-T. Phan, P.-N. Nguyen, T.-T. Dang, T.-N. Tran, D.-T. Vo, V.-K. Nguyen and M.-T. Dao, *Arch. Environ. Contam. Toxicol.*, 2024, **86**, 48–57.
- 71 L.-T.-T.-T. Hoang, H.-V.-T. Phan, N.-N. Nguyen, T.-T. Dang, T.-N. Tran, V.-K. Nguyen and M.-T. Dao, *Int. J. Phytorem.*, 2024, 1–12.
- 72 D. B. Thinh, N. T. Tien, N. M. Dat, H. H. T. Phong, N. T. H. Giang, D. T. Y. Oanh, H. M. Nam, M. T. Phong and N. H. Hieu, *Synth. Met.*, 2020, **270**, 116583.
- 73 M. Muniyalakshmi, K. Sethuraman and D. Silambarasan, *Mater. Today: Proc.*, 2020, **21**, 408–410.
- 74 P. Moradi and M. Hajjiami, *RSC Adv.*, 2021, **11**, 25867–25879.
- 75 J. Li, J. Guo and H. Dai, *Sci. Adv.*, 2022, **8**, eabo0399.
- 76 R. Md Salim, J. Asik and M. S. Sarjadi, *Wood Sci. Technol.*, 2021, **55**, 295–313.
- 77 N. T. Tin, N. T. T. Huyen, P. M. Tu, P. P. D. Minh, N. T. H. Nam, C. Q. Cong, N. D. Hai, H. An, N. M. Dat and H. T. Duong, *Mater. Lett.*, 2023, **342**, 134304.
- 78 X. Li, D. Zeng, P. Ke, G. Wang and D. Zhang, *RSC Adv.*, 2020, **10**, 7163–7169.
- 79 N. T. T. Van, P.-a. Gaspillo, H. G. T. Thanh, N. H. T. Nhi, H. N. Long, N. Tri, N. T. T. Van, T.-T. Nguyen and H. K. P. Ha, *Heliyon*, 2022, **30**, 103041.
- 80 D. L. T. Cuong, D. N. Trinh, N. T. T. Linh, N. D. Hai, P. T. L. Chau, N. T. Hoang, M. T. Phong and N. H. Hieu, *Mater. Res. Bull.*, 2022, **156**, 112000.
- 81 P. W. Albers, V. Leich, A. J. Ramirez-Cuesta, Y. Cheng, J. Hönig and S. F. Parker, *Mater. Adv.*, 2022, **3**, 2810–2826.
- 82 D. Li, J. Huang, L. Huang, S. Tan and T. Liu, *Langmuir*, 2021, **37**, 1521–1530.
- 83 P. Moradi, *RSC Adv.*, 2022, **12**, 33459–33468.
- 84 N. A. D. Ms, S. N. Ms, S. S. Mr, R. B. Ms, S. R. Ms, W. I. S. Mr and B. P. Swain, *Diamond Relat. Mater.*, 2020, **104**, 107756.
- 85 J. Geng, Y. Men, C. Liu, X. Ge and C. Yuan, *RSC Adv.*, 2021, **11**, 16592–16599.
- 86 U. P. Agarwal, *Front. Plant Sci.*, 2014, **5**, 490.
- 87 R. S. Dassanayake, N. Dissanayake, J. S. Fierro, N. Abidi, E. L. Quitevis, K. Boggavarappu and V. D. Thalangamaarachchige, *Appl. Spectrosc. Rev.*, 2023, **58**, 180–205.
- 88 S. Prabhu, L. Cindrella, O. J. Kwon and K. Mohanraju, *Sol. Energy Mater. Sol. Cells*, 2017, **169**, 304–312.
- 89 E. A. Bakr, M. N. El-Nahass, W. M. Hamada and T. A. Fayed, *RSC Adv.*, 2021, **11**, 781–797.
- 90 M. Aghaei-Hashjin, A. Yahyazadeh and E. Abbaspour-Gilandeh, *RSC Adv.*, 2021, **11**, 23491–23505.
- 91 J. Gupta, P. Hassan and K. Barick, *AIP Adv.*, 2021, **11**, 025207.



- 92 A. Zaman, J. T. Orasugh, P. Banerjee, S. Dutta, M. S. Ali, D. Das, A. Bhattacharya and D. Chattopadhyay, *Carbohydr. Polym.*, 2020, **246**, 116661.
- 93 K. Phasuksom, W. Prissanaroon-Ouajai and A. Sirivat, *RSC Adv.*, 2020, **10**, 15206–15220.
- 94 W. Li, M. Xu, Q. Cao, J. Luo, S. Yang and G. Zhao, *RSC Adv.*, 2021, **11**, 19387–19394.
- 95 F. Asghar, B. Shakoor, S. Fatima, S. Munir, H. Razzaq, S. Naheed and I. S. Butler, *RSC Adv.*, 2022, **12**, 11750–11768.
- 96 A. G. de Souza, R. F. Barbosa and D. S. Rosa, *J. Polym. Environ.*, 2020, **28**, 1851–1868.
- 97 O. Akatwijuka, M. A.-H. Gepreel, A. Abdel-Mawgood, M. Yamamoto, Y. Saito and A. H. Hassanin, *Biomass Convers. Biorefin.*, 2024, **14**, 7449–7465.
- 98 G. Flores-Jerónimo, J. Silva-Mendoza, P. Morales-San Claudio, A. Toxqui-Terán, J. Aguilar-Martínez and L. Chávez-Guerrero, *Waste Biomass Valorization*, 2021, 1–9.
- 99 H.-A. S. Tohamy, M. El-Sakhawy and S. Kamel, *J. Renewable Mater.*, 2022, **10**, 1889.
- 100 K. K. Khichar, S. B. Dangi, V. Dhayal, U. Kumar, S. Z. Hashmi, V. Sadhu, B. L. Choudhary, S. Kumar, S. Kaya and A. E. Kuznetsov, *Polym. Compos.*, 2020, **41**, 2792–2802.
- 101 X. Wei, T. Huang, J.-h. Yang, N. Zhang, Y. Wang and Z.-w. Zhou, *J. Hazard. Mater.*, 2017, **335**, 28–38.
- 102 K. Ali, A. K. Sarfraz, I. M. Mirza, A. Bahadur, S. Iqbal and A. ul Haq, *Curr. Appl. Phys.*, 2015, **15**, 925–929.
- 103 V. S. Munagapati, H.-Y. Wen, Y. Vijaya, J.-C. Wen, J.-H. Wen, Z. Tian, G. M. Reddy and J. Raul Garcia, *Int. J. Phytorem.*, 2021, **23**, 911–923.
- 104 J. L. Colaizzi and P. R. Klink, *J. Pharm. Sci.*, 1969, **58**, 1184–1189.
- 105 M.-T. Dao, T.-P.-L. Tran, D.-T. Vo, V.-K. Nguyen and L.-T.-T.-T. Hoang, *Adv. Mater. Sci. Eng.*, 2021, **2021**, 1–10.
- 106 B. N. Mahato, T. Krithiga and M. M. Thangam, *Surf. Interfaces*, 2021, **23**, 100636.
- 107 V. S. Munagapati, H.-Y. Wen, J.-C. Wen, A. R. Gollakota, C.-M. Shu, K.-Y. A. Lin and J.-H. Wen, *Int. J. Phytorem.*, 2022, **24**, 131–144.
- 108 S. S. Ray, R. Gusain and N. Kumar, *Carbon Nanomaterial-Based Adsorbents for Water Purification: Fundamentals and Applications*, Elsevier, 2020.
- 109 S. Figaro, J. P. Avril, F. Brouers, A. Ouensanga and S. Gaspard, *J. Hazard. Mater.*, 2009, **161**, 649–656.
- 110 Y. S. Ho and G. McKay, *Process Biochem.*, 1999, **34**, 451–465.
- 111 S. Y. Elovich, O. Larinov, I. Akad, N. SSSR and O. Khim, *Nauk*, 1962, **2**, 209–216.
- 112 J. Wang and X. Guo, *J. Hazard. Mater.*, 2020, **390**, 122156.
- 113 C. Aharoni and F. Tompkins, in *Advances in Catalysis*, Elsevier, 1970, vol. 21, pp. 1–49.
- 114 F.-C. Wu, R.-L. Tseng and R.-S. Juang, *Chem. Eng. J.*, 2009, **150**, 366–373.
- 115 I. Langmuir, *J. Am. Chem. Soc.*, 1916, **38**, 2221–2295.
- 116 H. Freundlich, *Z. Phys. Chem.*, 1907, **57**, 385–470.
- 117 R. Sips, *J. Chem. Phys.*, 1948, **16**, 490–495.
- 118 M. I. Temkin and Zh. Fiz, *Chim.*, 1941, **15**, 296–332.
- 119 A. W. Adamson and A. P. Gast, *Physical Chemistry of Surfaces*, Interscience publishers, New York, 1967.
- 120 M. A. Al-Ghouti and D. A. Da'ana, *J. Hazard. Mater.*, 2020, **393**, 122383.
- 121 R.-L. Tseng and F.-C. Wu, *J. Hazard. Mater.*, 2008, **155**, 277–287.
- 122 R. Sips, *J. Chem. Phys.*, 1948, **16**, 490–495.
- 123 T. A. Saleh, in *Interface Science and Technology*, ed. T. A. Saleh, Elsevier, 2022, vol. 34, pp. 99–126.
- 124 A. A. Oladipo, M. A. Abureesh and M. Gazi, *Int. J. Biol. Macromol.*, 2016, **90**, 89–99.
- 125 X. Li and J. Shi, *Chemosphere*, 2022, **293**, 133574.
- 126 L. Chen, H. Yang, R. Hong, X. Xie, R. Zuo, X. Zhang, S. Chen, D. Xu and Q. Zhang, *J. Environ. Chem. Eng.*, 2024, 114121.
- 127 J. Wang, R. Liu and X. Yin, *J. Chem. Eng. Data*, 2018, **63**, 409–416.
- 128 M. A. Ahmed, M. A. Ahmed and A. A. Mohamed, *React. Funct. Polym.*, 2023, **191**, 105701.
- 129 Q. Yao, B. Fan, Y. Xiong, C. Jin, Q. Sun and C. Sheng, *Sci. Rep.*, 2017, **7**, 45914.
- 130 A. Chowdhury, S. Kumari, A. A. Khan, M. R. Chandra and S. Hussain, *Colloids Surf., A*, 2021, **611**, 125868.
- 131 A. Nasiri, S. Rajabi, A. Amiri, M. Fattahizade, O. Hasani, A. Lalehzari and M. Hashemi, *Arabian J. Chem.*, 2022, **15**, 104014.
- 132 Q. Liao, H. Rong, M. Zhao, H. Luo, Z. Chu and R. Wang, *J. Hazard. Mater.*, 2022, **422**, 126863.
- 133 R. Rehman and S. Majeed, *Int. J. Phytorem.*, 2022, **24**, 1004–1013.
- 134 M. K. Uddin, N. N. Abd Malek, A. H. Jawad and S. Sabar, *Int. J. Phytorem.*, 2023, **25**, 393–402.

